The Effects of Ambient Conditions on Helicopter Harmonic Noise Radiation: Theory and Experiment

Eric Greenwood
Aeroacoustics Branch
NASA Langley Research Center
Hampton, VA

Ben W. Sim
US Army Aviation Development Directorate
Aviation & Missile Research, Development & Engineering Center
Research, Development and Engineering Command
Moffett Field, CA

D. Douglas Boyd, Jr.
Aeroacoustics Branch
NASA Langley Research Center
Hampton, VA

ABSTRACT

The effects of ambient atmospheric conditions, air temperature and density, on rotor harmonic noise radiation are characterized using theoretical models and experimental measurements of helicopter noise collected at three different test sites at elevations ranging from sea level to 7000 ft above sea level. Significant changes in the thickness, loading, and blade-vortex interaction noise levels and radiation directions are observed across the different test sites for an AS350 helicopter flying at the same indicated airspeed and gross weight. However, the radiated noise is shown to scale with ambient pressure when the flight condition of the helicopter is defined in nondimensional terms. Although the effective tip Mach number is identified as the primary governing parameter for thickness noise, the nondimensional weight coefficient also impacts lower harmonic loading noise levels, which contribute strongly to low frequency harmonic noise radiation both in and out of the plane of the horizon. Strategies for maintaining the same nondimensional rotor operating condition under different ambient conditions are developed using an analytical model of single main rotor helicopter trim and confirmed using a CAMRAD II model of the AS350 helicopter. The ability of the Fundamental Rotorcraft Acoustics Modeling from Experiments (FRAME) technique to generalize noise measurements made under one set of ambient conditions to make accurate noise predictions under other ambient conditions is also validated.

NOTATION

A	Rotor disc area, ft^2 (m^2).
a	Blade sectional lift curve slope.
a_0	Ambient speed of sound, ft/s (m/s).
C_H	Main rotor "H-force" coefficient.
C_{M_x}	Fuselage rolling moment coefficient.
C_{M_y}	Fuselage pitching moment coefficient.
$C_{p'}$	Acoustic pressure coefficient, $p'/\rho_0 a_o^2$.
$C_{p_{ij}}$	Blade surface pressure coefficient, $p_{ij}/\rho_0\Omega^2R^2$.
C_Q	Main rotor torque coefficient.
C_T	Main rotor thrust coefficient.
C_W	Main rotor weight coefficient.
C_Y	Main rotor lateral force coefficient.
c_{d_0}	Blade sectional drag coefficient.
D	Parasite drag, lbf (N).
f	Effective flat plate drag area, ft^2 (m^2).
H	Rotor "H-force", lbf (N).
$\bar{h}$	Nondimensional rotor mast height.
$\bar{l}$	Nondimensional tail rotor boom length.
M	Blade element Mach number.
M_{AT}	Main rotor advancing tip Mach number.
M_H	Main rotor hover tip Mach number.
M_{H_e}	Effective hover tip Mach number.
M_n	Mach number normal to surface.
M_r	Mach number in propagation direction.
$\vec{n}$	Blade surface normal.
p_{ij}	Blade element surface pressure, Pa.
p'	Acoustic perturbation pressure, Pa.
p_0	Ambient (station) pressure, Pa.
p_{SL}	Sea level ambient pressure, Pa.
Q_{ij}	Lighthill stress tensor, Pa.
R	Rotor radius, ft (m).
R_*	Gas constant for air.
r	Propagation distance, ft (m).
$\bar{r}$	Propagation distance in rotor radii, r/R.
$\mathfrak{r}$	Blade element radial station in rotor radii.
$\bar{S}$	Nondimensional surface area, S/R^2.
T	Thrust, lbf (N).
T_0	Air temperature, °F (K).
t	Observer time, s.
$\bar{t}$	Nondimensional observer time, $t\Omega$.
u	Fluid velocity, ft/s (m/s).
v	Blade element velocity, ft/s (m/s).
V	True airspeed, kts.
V_{IAS}	Indicated airspeed, kts.
W	Weight, lbf (N).
Y	Main rotor lateral force, lbf (N).
$\vec{x}$	Observer location in rotor radii.
$\bar{x}_c$	Nondimensional longitudinal CG location.
$\bar{y}_c$	Nondimensional lateral CG location.
α	Rotor tip-path-plane angle of attack, rad. (deg.).
β_0	Coning angle, rad. (deg.).
β_{1c}	Longitudinal blade flapping angle, rad. (deg.).

Presented at the American Helicopter Society 72nd Annual Forum, West Palm Beach, FL, May 17-19, 2016.

β_{1s} Lateral blade flapping angle, rad. (deg.).
β_p Blade precone angle, rad. (deg.).
γ Flight path angle, rad. (deg.).
γ_b Lock number.
γ_* Adiabatic coefficient of air.
θ Fuselage pitch angle, rad. (deg.).
θ_0 Collective pitch angle, rad. (deg.).
θ_{1c} Lateral cyclic blade pitch angle, rad. (deg.).
θ_{1s} Longitudinal cyclic blade pitch angle, rad. (deg.).
θ_r Observer angle.
θ_s Main rotor shaft pitch angle, rad. (deg.).
θ_{tw} Rotor blade twist.
Λ Local blade element surface slope.
$\bar{\Lambda}$ Airfoil shape factor.
λ_i Induced inflow ratio.
μ Main rotor advance ratio.
μ_x Tangential main rotor advance ratio.
μ_z Perpendicular main rotor advance ratio.
ν_β Rotating flap frequency.
ρ_0 Ambient air density, slug/ft^3.
ρ_{SL} Ambient air density at sea level, slug/ft^3.
σ Main rotor solidity.
ϕ Fuselage roll angle, rad. (deg.).
ϕ_s Main rotor shaft roll angle, rad. (deg.).
ψ Rotor azimuth angle, rad. (deg.).
χ Wake skew ratio.
Ω Main rotor rotational speed, rad./s.
ω_β Non-rotating flap frequency.

INTRODUCTION

Helicopter operators are increasingly interested in the acoustic impact of their operations. For military operators, detection of helicopters by hostile forces is often triggered by acoustic emissions, making acoustics a key element of mission survivability. For civil operators, helicopter noise drives community annoyance of helicopter operations resulting in complaints. In response, local and national governments are increasingly pressured to limit helicopter operations in noise sensitive communities. The negative impacts of helicopter noise can be mitigated by incorporating acoustic analysis into mission planning tools, allowing operators to design missions that reduce acoustic impacts while still effectively completing the mission objectives.

Helicopter Source Noise Modeling

Several empirical helicopter source noise modeling methods are currently in use. The simplest is derived from noise-power-distance extrapolations of measured data at a few microphone locations in order to capture some information about the directivity of helicopter noise (Ref. 1). More complex modeling methods are based on a linear (Refs. 2–4) or planar (Refs. 5, 6) grid of ground-based microphones—with the most complex of these methods measuring the radiated noise from a maneuvering helicopter in many directions simultaneously using a dense array of microphone positions on the ground (Ref. 6). All of these modeling approaches have one thing in common—they are based upon acoustic measurements at a single ambient operating condition. Changes in that ambient condition are either not considered or are accounted for indirectly (and perhaps incorrectly) through changes in the other input parameters to the model.

Although helicopters typically operate close to the ground, they regularly operate from bases at varied elevations where the ambient conditions differ significantly from standard sea level conditions. Existing land-use and mission planning tools based on empirical source noise models, such as the widely used Rotorcraft Noise Model (RNM) (Refs. 2, 3), generally neglect the effects of ambient conditions on helicopter noise sources. The Federal Aviation Administration's Heliport Noise Model (HNM) (Ref. 7) does include an empirical correction to data measured during the reference flyover flight condition based on the nondimensional advancing tip Mach number; this is used to adjust the source noise level of the measured flight condition for airspeeds other than that measured, but because the correction is formulated in terms of the nondimensional advancing tip Mach number, it also includes the effect of temperature changes by way of changes in the ambient speed of sound. However, the simple second order polynomial curve fit used by the HNM method does not fully account for the changes in rotorcraft noise sources due to both flight and ambient condition changes, nor can the integrated modeling method capture changes in the directivity of noise due to changes in operating condition (Ref. 8).

Effects of Ambient Conditions on Helicopter Harmonic Noise Radiation

The rotor operating condition is defined by a set of four independent and nondimensional parameters, which are known (Refs. 9–11) through theory and experiment to govern the rotor harmonic noise sources. These parameters may be defined as the rotor advance ratio, μ, advancing tip Mach number, M_{AT}, wake skew ratio, χ, and rotor thrust coefficient, C_T.

Consider the Ffowcs Williams – Hawkings (Ref. 12) equation, commonly used to calculate the acoustic effect of the aerodynamic sources that cause helicopter noise:

$$
\begin{aligned}
p'(x,t) = & \frac{1}{4\pi}\frac{\partial}{\partial t}\int_S \left[\frac{\rho_0 v_n}{r|1-M_r|}\right]_{ret} dS && \text{(monopole)} \quad (1)\\
& -\frac{1}{4\pi}\frac{\partial}{\partial x_i}\int_S \left[\frac{P_{ij}n_j}{r|1-M_r|}\right]_{ret} dS && \text{(dipole)}\\
& +\frac{1}{4\pi}\frac{\partial^2}{\partial x_i x_j}\int_V \left[\frac{Q_{ij}}{r|1-M_r|}\right]_{ret} dV && \text{(quadrupole)}
\end{aligned}
$$

Following Schmitz et al., (Ref. 9), this equation may be recast in nondimensional form for rotor noise sources by nondimensionalizing all geometric terms by the rotor radius, R, and temporal terms by the rotor azimuth angle, ψ. Retaining only

the "on-surface" monopole and dipole terms that cause thickness and loading noise, respectively, the resulting nondimensional Ffowcs Williams – Hawkings equation is:

$$C_{p'}(\bar{x},\bar{t}) = \frac{p'(\bar{x},\bar{t})}{\rho_0 a_0^2} = \frac{1}{4\pi} M_H \frac{\partial}{\partial \bar{t}} \int_{\bar{S}} \frac{M_n}{\bar{r}(1-M_r)} d\bar{S} - \frac{1}{4\pi} \frac{\partial}{\partial \bar{x}_i} \int_{\bar{S}} \frac{C_{p_{ij}} n_j M^2}{\bar{r}(1-M_r)} d\bar{S} \quad (2)$$

where the blade surface pressures are nondimensionalized by the dynamic pressure at the respective blade element:

$$C_{p_{ij}} = \frac{p_{ij}}{\rho_0 u^2(\mathfrak{r},\psi)} \quad (3)$$

The source terms in this equation are dependent only on the rotor geometry, motion, and aerodynamic state, which are uniquely defined by the governing parameters μ, M_{AT}, χ, and C_T. This result implies that the radiated acoustic pressure should scale in proportion to $\rho_0 a_0^2$—and likewise the ambient pressure—if the governing nondimensional parameters of the rotor are held constant. This approach was used previously to correct in-flight acoustic data for the S-76C helicopter measured at altitude by the YO-3 aircraft to acoustic measurements of a full-scale S-76 rotor in the 80- by 120- foot National Full-Scale Aerodynamics Complex (NFAC) wind tunnel at NASA Ames Research Center (Ref. 13).

In practice, the flight condition of the helicopter is usually defined by operators and mission planners in terms of dimensional parameters that can be directly measured, such as the indicated airspeed, V_{IAS}, gross weight, W, and flight path angle, γ. However, these parameters result in different values for the nondimensional governing parameters for acoustics, depending on the ambient air density and temperature. Figure 1 plots how these parameters vary for the AS350 helicopter in 80 Knots Indicated Airspeed (KIAS) flight at constant weight and rotor RPM as the ambient conditions change in response to changes in altitude above Mean Sea Level (MSL), as defined by the International Standard Atmosphere Model (Ref. 14). Equations relating the nondimensional governing parameters to the dimensional flight and ambient conditions are provided in the Appendix.

As ambient air density decreases with increasing altitude, the advance ratio, μ, must increase in order to maintain the same dynamic pressure and hence indicated airspeed, V_{IAS}. Likewise, the weight coefficient, C_W, increases with decreasing density. The advancing tip Mach number, M_{AT}, increases in response to decreasing temperature (and lower ambient speed of sound), but this is moderated by the increase in true airspeed for constant indicated airspeed. Only the wake skew ratio, χ, remains constant—this is primarily because the fuselage drag is held constant for constant indicated airspeed, and is therefore kept in proportion to the vehicle gross weight resulting in a constant rotor tip-path-plane angle of attack. A previous paper by Greenwood and Schmitz (Ref. 15) predicted significant changes in rotor harmonic noise in response to changes in these governing parameters using a physics-based model of the helicopter main rotor aerodynamics and acoustics—however, data were not available at that time to validate those predictions.

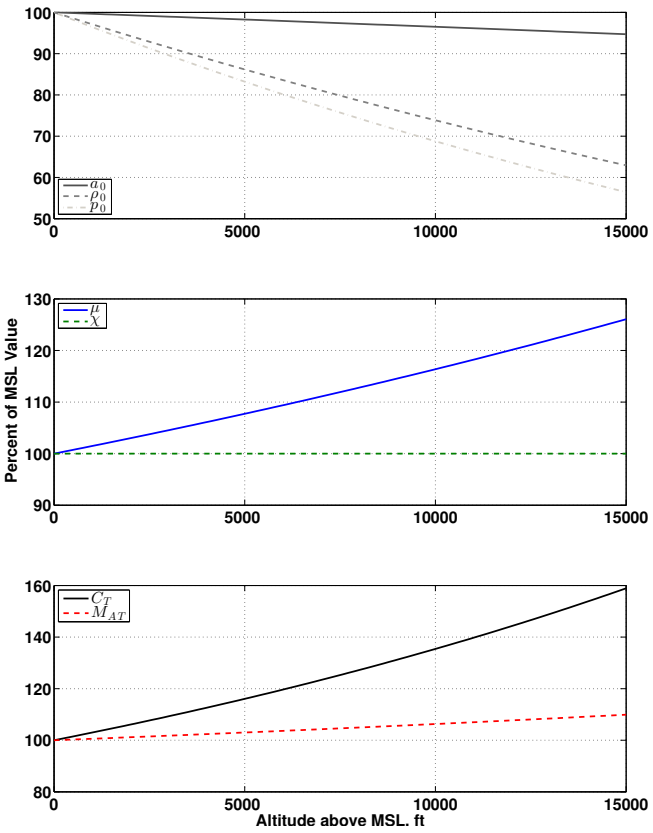

Fig. 1. Variations in the nondimensional governing parameters of rotor harmonic noise radiation for the AS350 helicopter flying at a constant 80 KIAS flight condition at various altitudes above mean sea level under International Standard Atmosphere ambient conditions.

In response to these concerns about the effects of ambient conditions on rotor harmonic noise radiation, a flight test campaign was conducted by NASA and the US Army Aeroflightdynamics Directorate to collect acoustic measurements for helicopters under different ambient conditions from September 2014 to February 2015. Noise data were collected for the AS350 SD1 and EH-60L at three different test sites across the Sierra Nevada mountain range at elevations of 0, 4000, and 7000 feet. Ambient temperatures ranged from 30 °F to 75 °F and density-altitudes from -700 ft to +8500 ft. The AS350 SD1 was selected in order to provide an open data set that could be used to validate acoustic prediction codes. Understanding the experimental measurements for the AS350 SD1 in steady flight, and comparing them to the noise theory developed in Ref. 15 is the focus of this paper. A detailed overview of the entire flight test campaign, discussing both helicopters used in the test, the steady and maneuvering flight test procedures, and an analysis of run-to-run variability in the data, is provided in another paper (Ref. 16).

Figure 2 shows the OverAll Sound Pressure Level (OASPL) noise contours on the surface of noise hemispheres generated using RNM's Acoustic Repropagation Technique (RNM/ART) (Ref. 3) for dimensionally-similar flight conditions at all three test sites. Indicated airspeeds range from 102-104 KIAS and

gross weights from 3970-4090 lbf. The noise contours are plotted using a Lambert projection; azimuth angles vary around the perimeter of the plot showing noise radiated towards the advancing (left) side at 90° azimuth, ahead of the helicopter towards 180° azimuth, and towards the retreating (right) side at 270°azimuth. Elevation angles are plotted from in the plane of the horizon, at 0° elevation to below the helicopter at −90° elevation. Data within 10° of the plane of the horizon are not available because the acoustic measurements are made from the ground. Significant differences in both noise levels and directivity can be observed between all three test sites.

OBJECTIVES

The main objective of this paper is to improve the understanding of the effects of ambient conditions on helicopter noise using both experimental measurements and a physics-based model of the helicopter based on the nondimensional scaling theory for rotor harmonic noise radiation. This paper will:

1. describe the measured changes in helicopter harmonic noise radiation due to changing ambient air density and temperature;
2. explain the physical mechanisms causing these changes in noise radiation using nondimensional noise scaling theory;
3. validate experimentally the nondimensional scaling of rotor harmonic noise radiation and;
4. demonstrate the application of this theory to estimate rotor harmonic noise radiation at various ambient conditions based on measurements obtained under a different ambient condition.

APPROACH

In order to measure the effects of changes in ambient conditions due to altitude variations (i.e., air density and temperature) on rotor noise generation, the flight conditions of the helicopters were defined in two different ways: dimensionally and nondimensionally.

The first set of flight conditions were defined in terms of a constant indicated airspeed and flight path angle, the dimensional parameters typically used by pilots and mission planners, and used to define conditions in previous acoustic flight tests. Three of these conditions were defined—one moderate speed level flight condition, one high speed level flight condition, and one moderate speed descending flight condition. By holding these dimensionally-defined flight conditions constant at all three test sites, the effects of changing altitude on noise radiation were directly measured for the manner in which helicopters are typically flown.

The second set of flight conditions were defined nondimensionally using the parameters that are believed to govern the acoustic state of the helicopter's rotors: the advancing tip Mach number, M_{AT}, the rotor advance ratio, μ, the rotor wake skew ratio, χ, and the weight coefficient, C_W. By putting the helicopter trim equations in nondimensional form, (see the Appendix for details), all four of these parameters can be matched

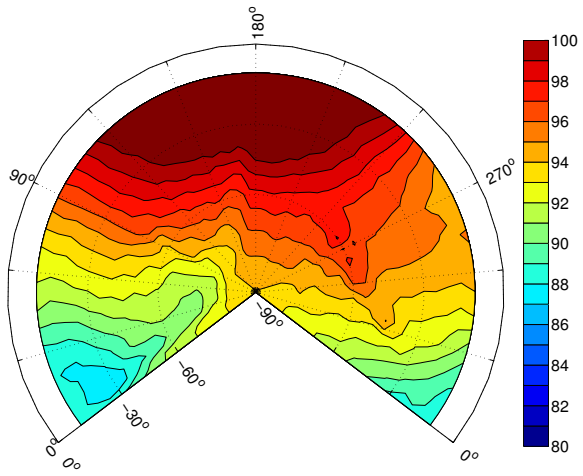

(a) RNM/ART hemisphere, 102.3 KIAS, Sea Level, dB OASPL.

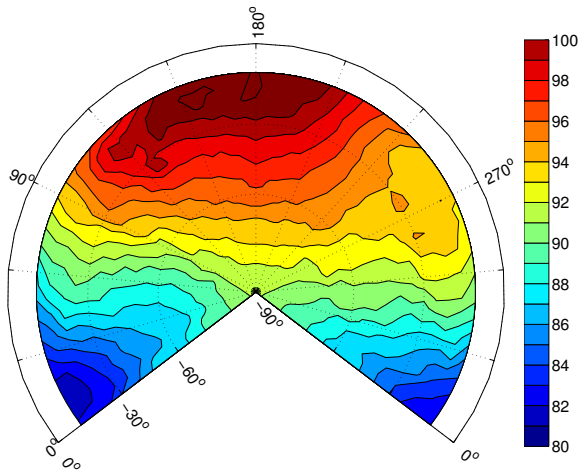

(b) RNM/ART hemisphere, 102.5 KIAS, 4000 ft MSL, dB OASPL.

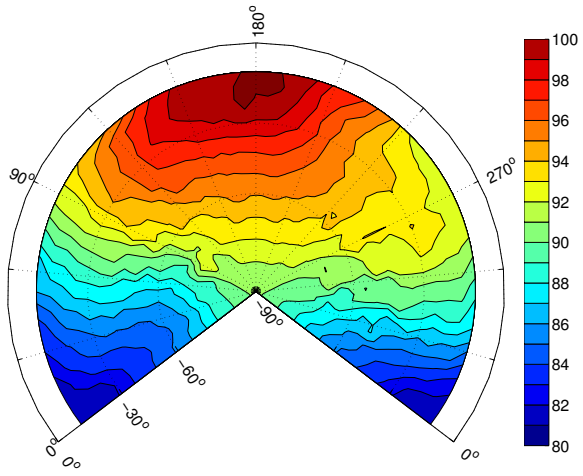

(c) RNM/ART hemisphere, 103.4 KIAS, 7000 ft MSL, dB OASPL.

Fig. 2. Measured noise hemispheres for 103 KIAS, $W \approx$ 4000 lbf flight conditions at each of the three test sites.

exactly for varying ambient air density and temperature by making adjustments to the indicated airspeed, rotor rotational speed, and weight of the vehicle. However, precise rotor speed control was not available for the AS350 SD1 helicopter, such that the advancing tip Mach number, M_{AT}, and the advance

ratio, μ, could not be varied independently in response to changes in the ambient speed of sound, a_0. Instead, flight conditions were defined in terms of Gopalan's effective hover tip Mach number, M_{H_e}. The effective hover tip Mach number is the hover tip Mach number, M_H, adjusted for Doppler amplification due to forward flight and was identified by Gopalan as the key scaling parameter for rotor thickness noise (Ref. 17). The effective hover tip Mach number can be expressed in terms of the rotor advance ratio, μ, and advancing tip Mach number, M_{AT}, using the expression:

$$M_{H_e} = \frac{M_{AT}}{1+\mu\,(1-M_{AT})} \tag{4}$$

For example, the thickness noise term of Equation 2 can be rearranged in terms of the effective hover tip Mach number, M_{H_e}, as follows:

$$C_{p'_T} = \frac{1}{4\pi}\frac{\partial}{\partial \bar{t}}\int_{\bar{S}} \frac{\Lambda M_{H_e}^2\,[\mathfrak{r}+\mu\sin\psi]}{\bar{r}\,[1+\mu M_{H_e}]^2\left(1-\frac{M_{H_e}[\mathfrak{r}+\mu\sin\psi]}{1+\mu M_{H_e}}\cos\theta_r\right)}\,d\bar{S} \tag{5}$$

Based on real-time measurements of the ambient density and temperature at the flight altitude, the dimensional flight condition of the helicopter was carefully adjusted to match the targeted M_{H_e} for these nondimensionally defined flight conditions. C_W was varied by targeting a take-off gross weight specific to the test conditions flown that day and tracking changes in weight due to fuel burn throughout the flight.

Direct measurements of the helicopter control positions were not available; however, the ability of this strategy to maintain a constant trim condition for the helicopter was confirmed by evaluating the trim solutions reached by a CAMRAD II model of the AS350 helicopter for a selection of the dimensionally defined and nondimensionally defined flight conditions flown at all three test sites during the altitude variation flight test campaign. The CAMRAD II model of the AS350 was adapted from a previously created model of the SA349/2 helicopter (Refs. 18, 19). The model was modified to match the geometric dimensions, fuselage and rotor blade mass properties of the AS350 helicopter. The CAMRAD II trim model contains many details that are not included in the nondimensional trim model provided in the Appendix. For instance, the blade masses cannot be changed in response to ambient conditions, so the nondimensional Lock number will vary with changes in the ambient density. The CAMRAD II trim results for several sets of descending flight conditions flown during the altitude variation test campaign are shown in Table 1.

The first three conditions are representative of the dimensionally-defined flight conditions flown during the test campaign. The indicated airspeed and weight are held constant between the test sites. For the most part, there is little variation in the predicted trim controls between the three cases. However, the rotor collective pitch, θ_0, increases in response to the increase in weight coefficient with decreasing ambient density. Conversely, the rotor longitudinal cyclic, θ_{1s}, decreases with increasing altitude. The second set of three flight conditions represent cases at constant weight coefficient and effective hover tip Mach number—however, there is a large variation in the ambient temperature between these conditions. Variations in collective pitch, θ_0, are minimized because the weight coefficient, C_W, is maintained between altitudes. However, due to the inability to precisely control rotor RPM, the airspeed must be varied in order to match the effective hover tip Mach number, M_{H_e}. As temperature decreases, true airspeed, V, must decrease to maintain the same effective hover tip Mach number, M_{H_e}. This causes a change in the relative balance between the drag of the helicopter and the weight, resulting in a more nose-up fuselage pitch attitude, θ, with decreasing air temperature. This also drives a corresponding change in the longitudinal cyclic pitch, θ_{1s}. However, if test points are selected with closely matching ambient air temperatures, variations are minimized across all of the trim parameters as air density changes with altitude, as shown in the third set of conditions listed in Table 1.

In this paper, the Fundamental Rotorcraft Acoustic Modeling from Experiments (FRAME) technique, developed by the first author, is used to generalize noise measurements made under one set of ambient conditions to other ambient conditions, see Ref. 20. FRAME constructs nondimensional analytical models of rotor noise radiation by fitting empirical parameters in the aerodynamic and acoustic models to match measured acoustic data from either wind tunnel tests, flight tests, or both. A flowchart of the method is shown in Figure 3. Wind tunnel measurements allow for more careful control of the operating state of the rotor over a wide range of operating conditions but are usually limited to scale models of isolated rotors. Flight test measurements are necessary to acquire noise data for the entire full-size vehicle, but for practical reasons the variations in operating condition are often limited. Because a physics-based model of the major rotor harmonic noise sources is constructed, noise estimates can be obtained at flight conditions and radiation directions that were not originally measured (Ref. 21).

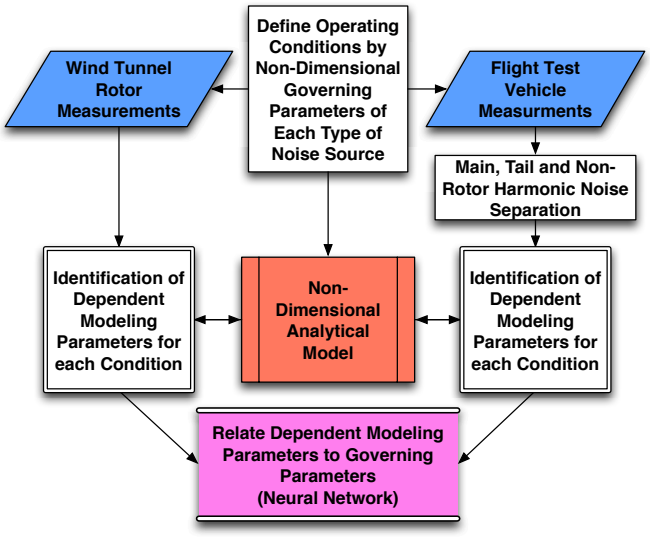

Fig. 3. Flowchart of the FRAME modeling method.

In the FRAME method, both types of experimental measurements of rotor noise are first classified by operating con-

	Altitude ft	ρ_0 slug/ft^3	T_0 °F	V_{IAS} kts	W lbf	M_{H_e} –	C_W –	θ_0 deg.	θ_{1s} deg.	θ_{1c} deg.	θ deg.	ϕ deg.
Dimensional	0	0.00231	67.7	**87.2**	**4113**	0.742	0.00352	3.98	1.52	1.06	-2.49	0.34
	4000	0.00208	53.7	**86.0**	**4075**	0.760	0.00387	4.33	1.21	1.07	-2.44	0.28
	7000	0.00186	54.3	**86.0**	**4113**	0.765	0.00440	4.97	0.66	1.13	-2.42	0.20
Constant M_{H_e}, C_W	0	0.00228	74.4	105.8	4338	**0.759**	**0.00379**	4.68	0.49	1.34	-3.48	0.18
	4000	0.00203	64.9	99.9	3855	**0.760**	**0.00379**	4.38	0.83	1.13	-2.88	0.29
	7000	0.00190	43.0	86.5	3624	**0.760**	**0.00379**	4.18	1.35	0.99	-2.08	0.37
Constant M_{H_e}, C_W, T_0	0	0.00229	**62.1**	99.0	4385	**0.761**	**0.00379**	4.48	0.89	1.22	-3.06	0.22
	4000	0.00205	**58.7**	91.2	3921	**0.759**	**0.00379**	4.43	0.87	1.13	-2.80	0.27
	7000	0.00185	**54.5**	84.9	3584	**0.762**	**0.00383**	4.41	0.87	1.03	-2.59	0.31

Table 1. CAMRAD II trim results for AS350 helicopter in γ = -6° descending flight.

dition in terms of the nondimensional governing parameters of rotor harmonic noise. For flight test measurements of an entire vehicle, the acoustic signals are transformed to a wind-tunnel reference frame using a time-domain de-Dopplerization technique (Ref. 22). The individual rotor blade passages can be identified from this signal, using the process illustrated in Figure 4. Starting from the de-Dopplerized signal (Fig. 4a), a wavelet power "spectrogram" is calculated for a number of wavelet scales clustered around the nominal main or tail rotor blade passage frequencies, as shown in Figure 4b. For each point in time, the maximum value of the wavelet power is taken to form the rotor blade passage detection signal, and normalized to a range from 0 to 1, as shown in Figure 4c. This signal contains two peaks per rotor blade passage, associated with the most positive and most negative peaks in the original pressure time history signal. Time windows associated with individual rotor blade passages can be identified by taking every other peak of this signal. These time windows are then applied to harmonically average the de-Dopplerized pressure time history signal, separating the contributions of main rotor, tail rotor, and non-rotor harmonic noise sources.

Using a parameter identification technique, analytical models of the rotor noise sources are then adapted to the acoustic measurements by adjusting a set of physically meaningful dependent modeling parameters to match the noise radiated for each set of nondimensional governing parameters. Application of the method across a wide range of operating conditions results in a set of dependent modeling parameters associated with the nondimensional governing parameters of the rotor noise sources. Using the dependent modeling parameters developed from flight test measurements of full vehicles and/or wind tunnel measurements of isolated rotors, a neural network model is employed to develop a functional relationship between the nondimensional governing and dependent modeling parameters over the entire range of operating conditions. By combining the neural network parameter estimator with the associated analytical model, estimates of noise at other operating conditions than those measured may be made.

The underlying analytical framework used in the FRAME model employs a Ffowcs Williams – Hawkings (FW-H) acoustic analogy method. Aerodynamic inputs are provided for each condition using a tunable prescribed wake model combined with an incompressible indicial unsteady aerodynamics model. The nondimensionalized form of the equation (Eq. 2) is solved numerically using Farassat Formulation 1A (Ref. 23). Thickness noise is directly computed from the blade geometry and rotor operating condition using Lopes' compact monopole approximation (Ref. 24), which may be rearranged in nondimensional form as:

$$C_{p'_T} = \frac{1}{4\pi} M_H^2 \int_0^1 \left(\frac{1}{|1-M_r|} \right)^2 \frac{\partial^2}{\partial \psi^2} \left(\frac{\bar{\Lambda}}{\bar{r}\,|1-M_r|} \right) d\mathfrak{r} \quad (6)$$

where $\bar{\Lambda}$ is the airfoil shape factor, approximately equal to the cross-sectional area of the airfoil nondimensionalized by R^2.

Acoustic sources off the blade surfaces, such as those causing High Speed Impulsive (HSI) noise, are neglected for the moderate advancing tip Mach number range examined in this paper. Loading noise, both lower harmonic and Blade-Vortex Interaction (BVI) noise, are solved from the compact-chord airloads determined from an assumed aerodynamic model adapted to measured data using parameter identification techniques. The aerodynamic model includes a wake model based on a modified Beddoes prescribed wake (Refs. 25, 26), where the dependent parameters adjusted by the FRAME method are used to describe: the nonuniform longitudinal and lateral inflow variations across the rotor disk, the initial vortex core size and its rate of growth (Ref. 27), the tip vortex rollup radius and the rate of wake contraction (Ref. 28), and the harmonic variation of vortex circulation strength about the rotor azimuth. The velocities induced by the wake onto the rotor blades are then corrected using the Beddoes-Leishman indicial aerodynamics model (Refs. 29, 30) to account for the delayed response of the shed wake on the rapidly changing aerodynamic loading felt by the blade elements. Airfoil aerodynamics data in the form of C81 tables can be used in the model. Airfoil data for the OA209 used in Refs. 18, 19 were applied to the AS350 modeled in this paper.

The FRAME model was calibrated to acoustic measurements for two different flight conditions at the sea level test site: a moderate speed level flight condition and a lower speed descending flight condition. The dimensional and nondimensional definitions of these conditions are listed in Table 2. The models were calibrated to harmonically averaged main and tail rotor waveforms produced from ground-based acoustic mea-

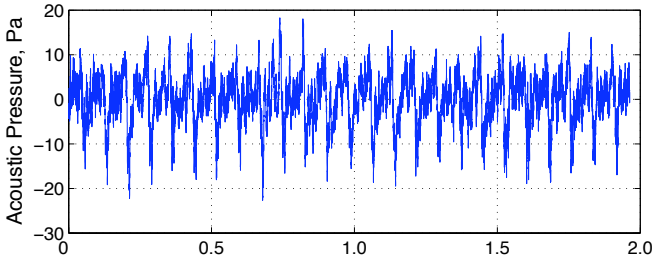

(a) De-Dopplerization of the pressure time history signal.

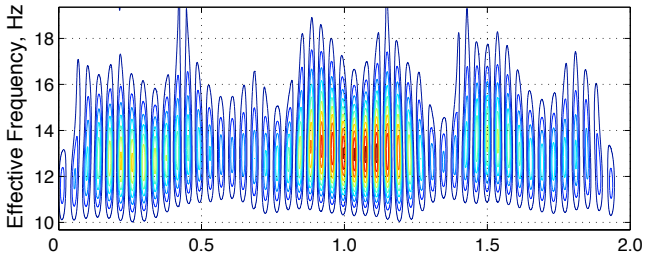

(b) Calculation of the wavelet power "spectrogram."

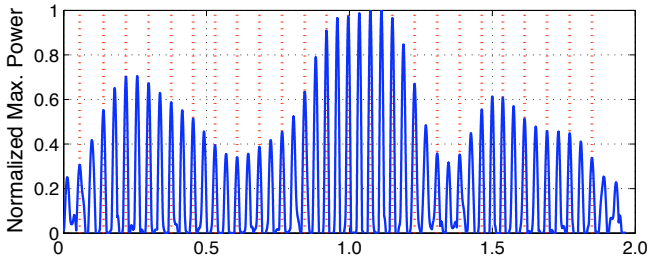

(c) Rotor blade passage time windows (red dashed) are detected from alternating peaks in the normalized maximum wavelet power signal.

Fig. 4. Acoustic period detection process as applied to the Bell 206 helicopter. (From Ref. 22)

surements. These waveforms were associated with the twelve directivity angles listed in Table 3.

V_{IAS} kts	W lbf	γ deg.	M_{H_e}	C_W
110.6	3942	0.3	0.791	0.0038
87.2	4113	-5.3	0.742	0.0035

Table 2. FRAME model calibration conditions.

RESULTS

Lower Harmonic Noise

The nondimensional acoustic pressure waveforms for an observer $11R$ away from the rotor hub and 10° below the plane of the horizon are compared for three flight conditions measured at each of the three test altitudes in Figure 5a. The waveforms were generated from the measured acoustic data by averaging the 80 blade passages nearest the target 10° emission angle. These flight conditions were selected from the range of available flight conditions to most closely match the nondimensional effective hover tip Mach number, M_{H_e}, and weight coefficient, C_W. Excellent agreement in the amplitude and pulse shape of the waveforms is observed, in accordance with the acoustic scaling theory for rotor harmonic noise.

Elevation deg.	Azimuth deg.
-10	120
-10	150
-10	180
-10	210
-10	250
-20	150
-25	180
-30	120
-40	105
-40	180
-40	255
-60	180

Table 3. Directivity angles used in FRAME model calibration.

The FRAME model was calibrated to the measured data for the sea level flight condition. The predicted waveform for this flight condition—including the separate contributions of the thickness and loading sources—is shown in Figure 5b. The negative pressure peak of the waveform is set by the thickness noise sources in the FRAME model. The asymmetry apparent in the positive peaks is caused by the lower harmonic loading noise sources. For this flight condition, the predicted tip-path-plane of the main rotor is tilted 12° below the horizon, nearly in the plane of the observer.

The OASPL hemisphere contours generated using RNM/ART for the sea-level calibration condition are plotted in Fig. 6a. The corresponding OASPL predicted using FRAME for all directivity angles below the horizon for this flight condition are shown in Fig. 6b. Good agreement is achieved between the measured and predicted noise levels across the forward directivity angles, where rotor harmonic noise from the main and tail rotors dominate. FRAME underpredicts noise levels towards the aft directivity angles, where significant non-rotor-harmonic noise occurs. These non-rotor-harmonic noise sources are not accounted for in the FRAME model and could result in underprediction of noise levels for some applications where observers are directly underneath and close to the helicopter, such as during noise certification. However, non-rotor-harmonic noise sources are not important for most helicopter noise impact analyses because the noise levels are much lower than those of the dominant main and tail rotor harmonic noise.

Figure 6c plots the OASPL contours generated using RNM/ART for a similar nondimensionally defined flight condition at the 7000 ft test site. While the overall directivity pattern shows close agreement to the sea level data plotted in Fig. 6a, the measured noise levels are somewhat lower in all directions. However, in accordance with Eq. 2, the noise levels are expected to decrease with increasing ambient pressure for

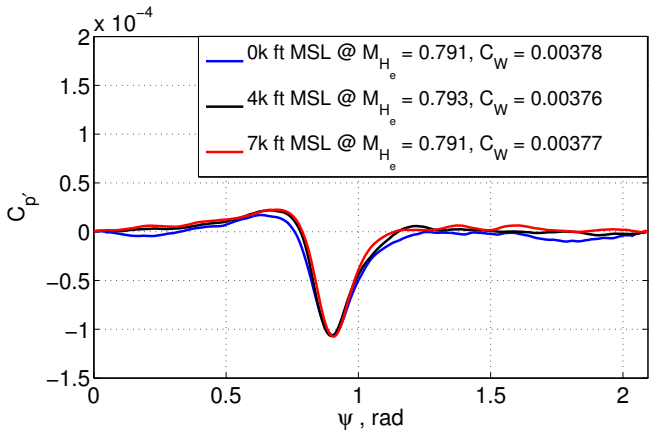

(a) Measured near-in-plane noise pulses.

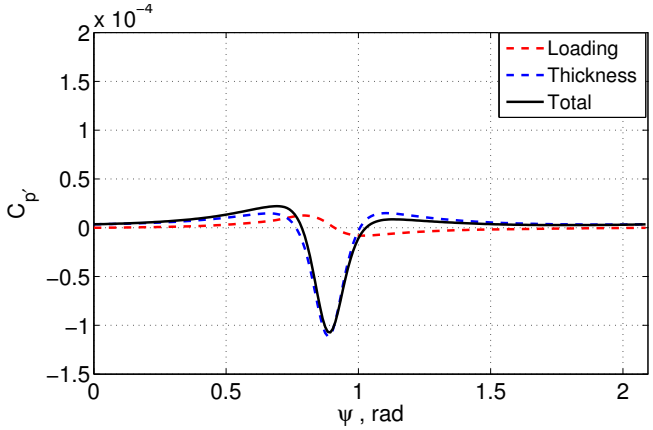

(b) FRAME calibrated near-in-plane noise pulse.

Fig. 5. Nondimensional near-in-plane main rotor noise pulses. (a) Comparison of measured near-in-plane main rotor waveforms for the same nondimensional operating condition at three different altitudes. (b) Calibrated noise prediction showing separated thickness and loading noise components.

the same rotor operating condition. The expected difference can be expressed as:

$$\Delta SPL = 20\log_{10}\frac{p_0}{p_{SL}} \tag{7}$$

Applying this equation to the RNM/ART hemisphere for the 7000 ft MSL flight condition to normalize it to the sea level ambient pressure results in the OASPL contours shown in Fig. 6d. The resulting noise levels for the 7000 ft MSL condition are in good agreement with the corresponding sea level case shown in Fig. 6a, confirming the nondimensional scaling theory developed in Boxwell et al. (Ref. 10).

Near-in-plane waveforms for dimensionally defined flight conditions at approximately the same indicated airspeed, V_{IAS}, and weight, W, are shown in Fig. 7a at each of the three test sites. For these conditions, a significant change in the magnitude of the negative pressure peak is observed as the ambient air density changes, nearly 6 dB between the highest and lowest test sites. Fig. 7b plots the variations in the main rotor noise radiation predicted by the FRAME model for the 110 KIAS level flight condition under the three sets of ambient conditions. The variation in predicted noise levels closely matches that measured. When accounting for the ambient pressure scaling to normalize the amplitudes to sea level equivalents, as expressed in Equation 7, the difference in the amplitudes of the measured waveforms is even larger.(Fig.7c)

Figure 8 plots the variation in the peak negative acoustic pressure coefficient of the waveform predicted by FRAME against measured values as a function of the effective hover tip Mach number, M_{H_e}. Because the observer is located directly ahead of the helicopter and near the plane of the rotor, the negative peak pressure is dominated by thickness noise sources. The measured data values are closely scattered about the predicted trend. M_{H_e} appears to be a good scaling parameter for thickness noise, as predicted by Gopalan's theory (Ref. 17).

Figure 9a shows the measured RNM/ART hemisphere OASPL contours for another level flight condition at 102.3 KIAS and a gross weight of 4092 lbf measured at the sea level test site. The corresponding FRAME prediction is shown in Fig. 9b. Once again, very good agreement is achieved between the measured and predicted noise levels near the plane of the horizon. Predicted out-of-plane noise levels are generally within 3 dB of measured levels. The RNM/ART hemisphere for a similar dimensionally defined flight condition at 7000 ft MSL altitude (103.4 KIAS, 3988 lbf.) is shown in Fig. 9c. A significant reduction is OASPL is observed in directions out of the plane of the horizon—similar results are seen in the FRAME predicted hemisphere shown in Fig. 9d—even though the weight coefficient, C_W, has increased from 0.0035 to 0.0042. Figure 9e shows the sea level hemisphere for a similar gross weight (3976 lbf), but with an effective hover tip Mach number, M_{H_e}, matching the 7000 ft MSL flight condition. Even though the tip Mach number is matched, higher noise levels can be observed out of the plane of the rotor and towards the advancing side of the helicopter. Similar trends are seen in the FRAME predictions shown in Fig. 9f.

Figure 10 compares the harmonically averaged pressure time history waveforms for an observer at 150° azimuth, −60° elevation, for the two cases with $M_{H_e} = 0.79$ but different C_W for constant gross weight shown in Fig. 9c and 9e. Both time history waveforms have the canonical shape of lower harmonic loading noise; however, an increase of nearly 6 dB in the amplitude of the waveforms can be observed in response to a 24% decrease in C_W. Conversely, the averaged tail rotor noise levels (Fig. 11) show a slight decrease between the higher and lower main rotor C_W conditions. This indicates that changes in the weight coefficient of the helicopter can result in acoustically significant changes in the trim of the helicopter, resulting in changes in the lower harmonic loading noise radiation in regions where thickness noise does not dominate. Moreover, these changes in lower harmonic loading noise do not simply scale directly in proportion to changes in rotor thrust—even for observers out-of-the-plane of the rotor—in contrast to the linearly proportional relationship between thrust and loading noise amplitudes that would be expected for an isolated rotor or propeller in axial flight.

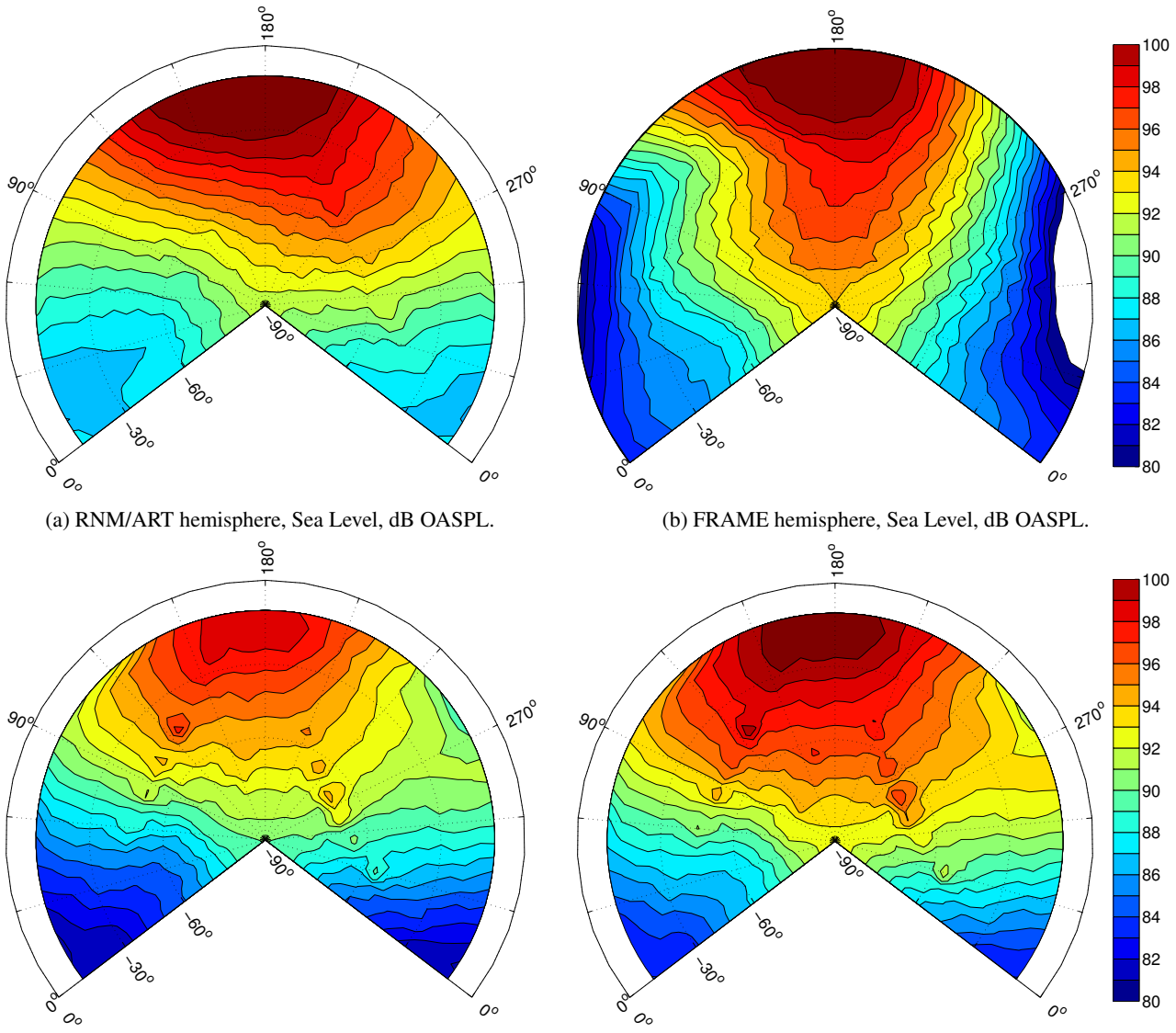

(a) RNM/ART hemisphere, Sea Level, dB OASPL.

(b) FRAME hemisphere, Sea Level, dB OASPL.

(c) RNM/ART hemisphere, 7000 ft MSL, dB OASPL.

(d) RNM/ART hemisphere, 7000 ft MSL re. Sea Level, dB OASPL.

Fig. 6. Measured, Predicted, and Scaled noise hemispheres for nondimensionally defined level flight calibration condition, M_{H_e} = 0.791, C_W = 0.0038.

Blade-Vortex Interaction Noise

Figure 12a plots the A-weighted Sound Pressure Level (A-SPL) contours for the descending flight FRAME sea level calibration condition of 87.2 KIAS and -5.3° flight path angle (γ) where there occurs significant BVI noise radiation. A strong BVI "hotspot" is observed radiating ahead of the helicopter, slightly towards the advancing side and -45° elevation below the horizon. Because of the relative unsteadiness of the descending flight cases, the FRAME steady flight condition is defined using the nondimensional parameter values calculated from the measured state moment at the precise time-of-emission associated with the peak A-weighted SPL value on the measured hemisphere. The FRAME model captures the amplitude and directivity of the dominant BVI noise, as shown in Fig. 12b. As was noted before, predicted noise levels are lower on the aft portion of the hemisphere, because non-rotor-harmonic noise sources are not modeled. The corresponding OASPL contours are shown for the RNM/ART hemisphere and FRAME prediction in Figs. 12c and 12d, respectively. The BVI noise still contributes to the OASPL levels; however, main and tail rotor lower harmonic noise contributions dominate the region near the plane of the horizon.

The harmonically averaged BVI noise pulse derived from the measured data corresponding to the peak A-weighted SPL direction on the hemisphere is shown in Fig. 13a. A strong positive pressure pulse is observed, followed by two smaller pressure peaks associated with weaker BVI originating from other parts of the rotor disk. The predicted FRAME BVI waveform is shown in Fig. 13b, and closely matches the overall shape and amplitude of the measured waveform, although the negative peak values of the BVI are overpredicted.

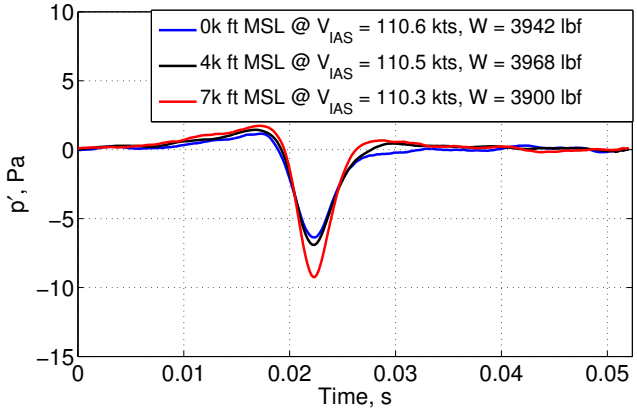

(a) Measured near-in-plane noise pulses.

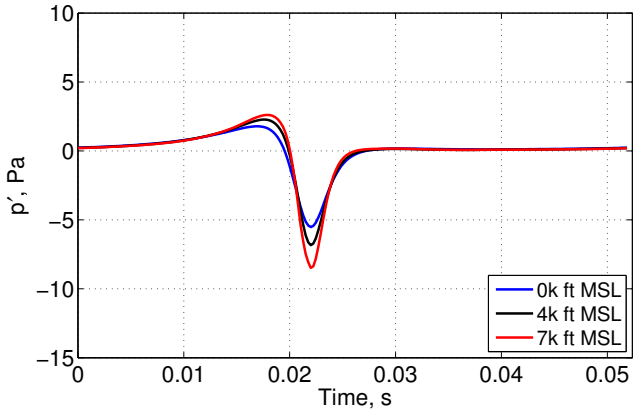

(b) FRAME predicted near-in-plane noise pulses.

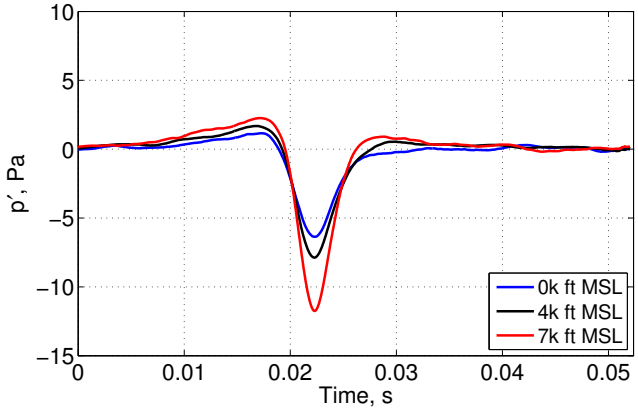

(c) Measured near-in-plane noise pulses scaled to sea level.

Fig. 7. Near-in-plane noise pulses for constant dimensionally-defined conditions at three different altitudes. (a) Comparison of measured near-in-plane main rotor waveforms for the same dimensional operating condition at three different altitudes. (b) Comparison of predicted waveforms at different altitudes. (c) Measured waveforms scaled to sea level pressure using Eq. 7.

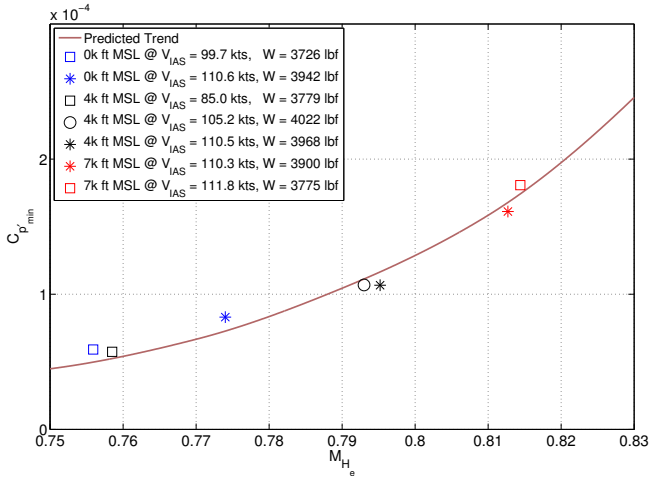

Fig. 8. Predicted and measured near-in-plane noise trend with varying M_{H_e}. The ✻ markers are the equivalent dimensional flight conditions from Fig. 7a, the ◯ marker is the calibration condition from Fig. 5a, and □ markers are from other measured level flight conditions collected during the experiment.

The A-weighted SPL noise contours for a similar dimensionally-defined descending flight condition (γ = -5.7°) at 7000 ft MSL altitude are plotted in Fig. 14a. A significant reduction in the peak BVI noise levels of about 3 dB can be observed relative to the sea level condition. The directivity of the radiated noise is further below the horizon than for the sea level case. The FRAME model accurately captures these changes, as shown in Fig. 14b.

CONCLUSIONS

Acoustic data collected for the AS350 helicopter flown at three different altitudes above mean sea level were analyzed in the paper. The results show that, when helicopters are operated under different ambient conditions, significant differences in noise radiation characteristics are observed for flight conditions at the same indicated airspeed, gross weight, and flight path angles. However, when flight conditions are defined in terms of the governing nondimensional parameters of rotor harmonic noise generation, μ, M_H, C_W, and χ, differences in noise radiation are accounted for through a simple scaling of acoustic pressures by local ambient pressure.

Using a simple nondimensional trim model, it was shown that the helicopter flight condition can be adjusted to match all four nondimensional governing parameters for any ambient conditions by varying the airspeed, vehicle gross weight, and rotor RPM. For vehicles such as the AS350, where precise rotor RPM control is not available, airspeeds can be adjusted to match Gopalan's effective hover tip Mach number, identified as a primary scaling parameter for rotor thickness and steady loading noise. CAMRAD II comprehensive analysis indicated that the other vehicle parameters, which cannot be readily scaled, such as the rotor blade properties, had very small effects on the overall helicopter trim condition.

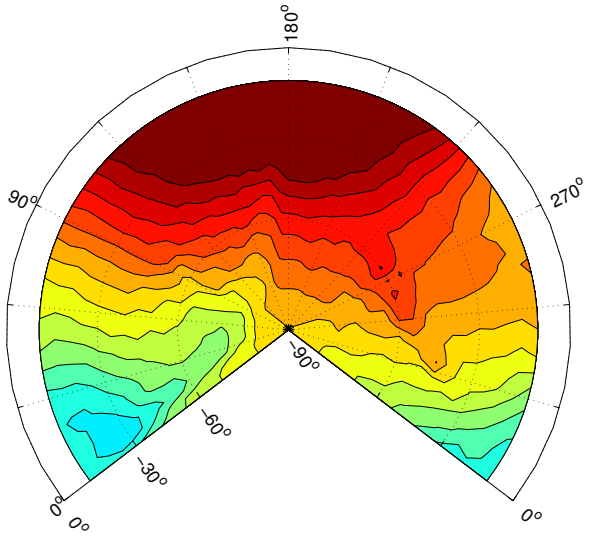

(a) RNM/ART hemisphere, 102.3 KIAS, Sea Level, dB OASPL.

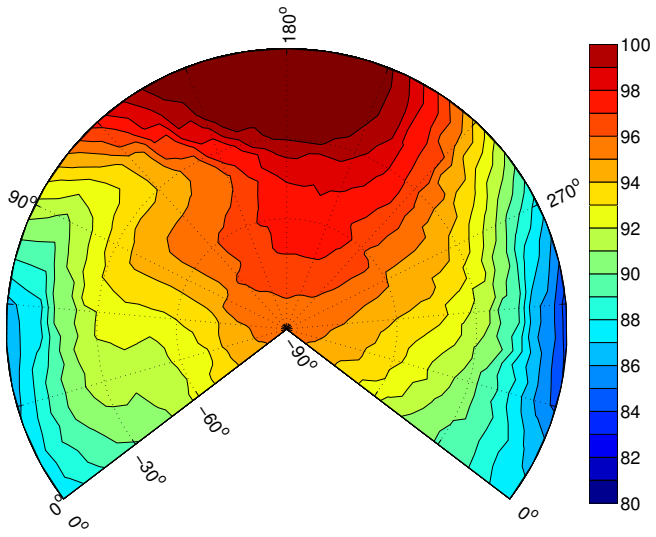

(b) FRAME hemisphere, 102.3 KIAS, Sea Level, dB OASPL.

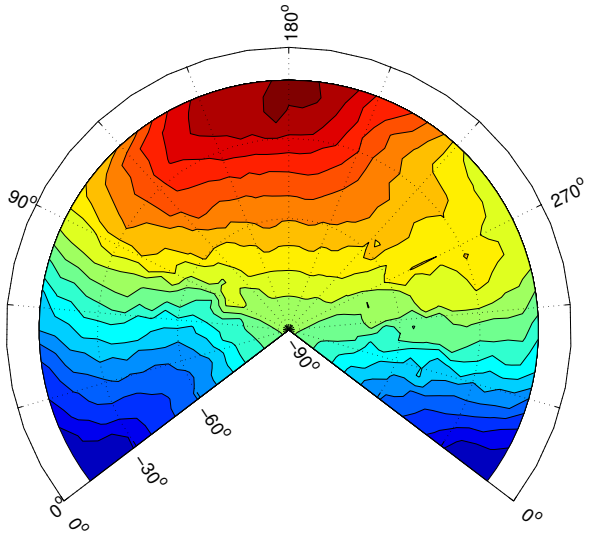

(c) RNM/ART hemisphere, 103.4 KIAS, 7000 ft MSL, dB OASPL.

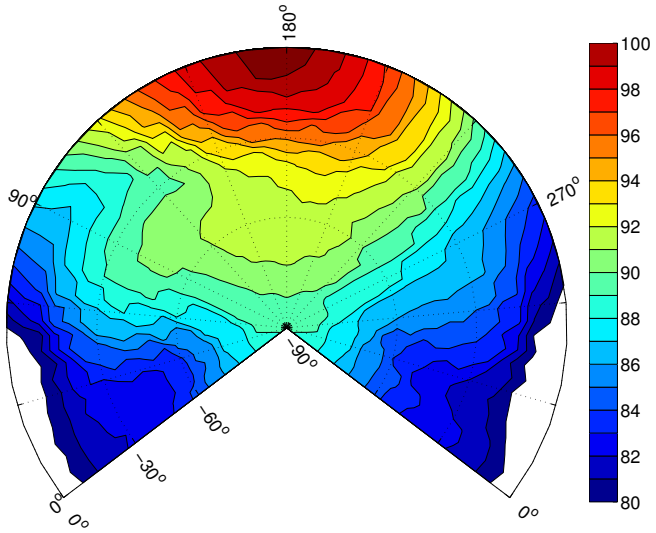

(d) FRAME hemisphere, 103.4 KIAS, 7000 ft MSL, dB OASPL.

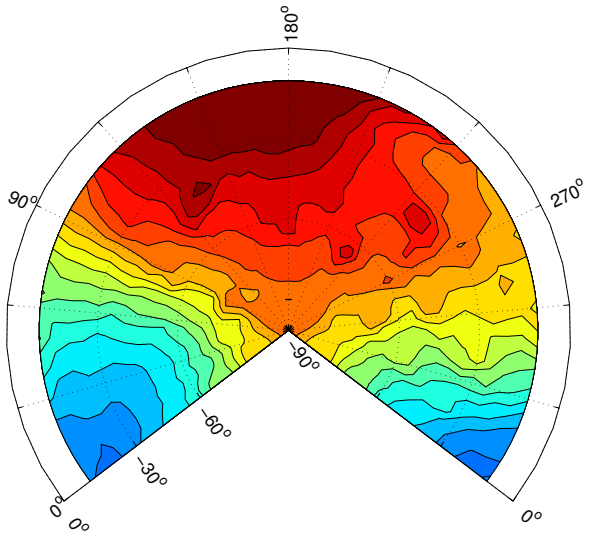

(e) RNM/ART hemisphere, 124.2 KIAS, Sea Level, dB OASPL.

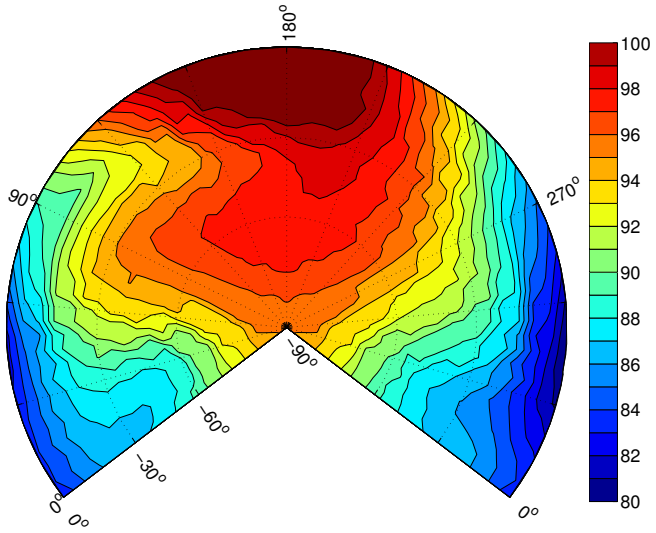

(f) FRAME hemisphere, 124.2 KIAS, Sea Level, dB OASPL.

Fig. 9. Measured and predicted noise hemispheres for $W \approx$ 4000 lbf flight conditions. (a-d) matched dimensional conditions. (c-f) matched M_he = 0.79, but C_W varies from (c-d) 0.0042 to (e-f) 0.0034.

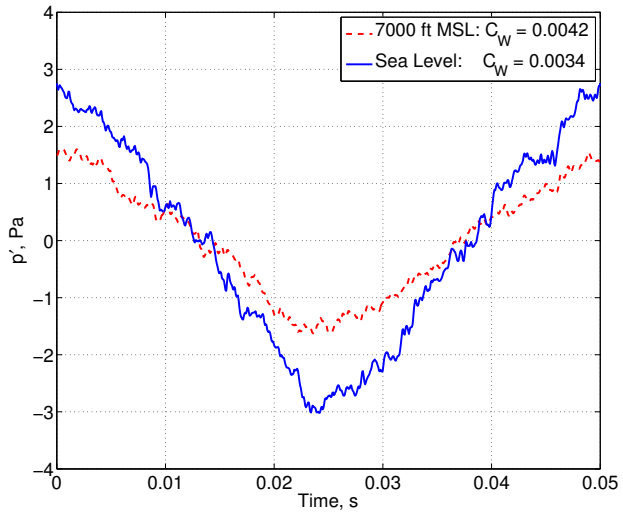

Fig. 10. Out-of-plane main rotor averaged pressure time history.

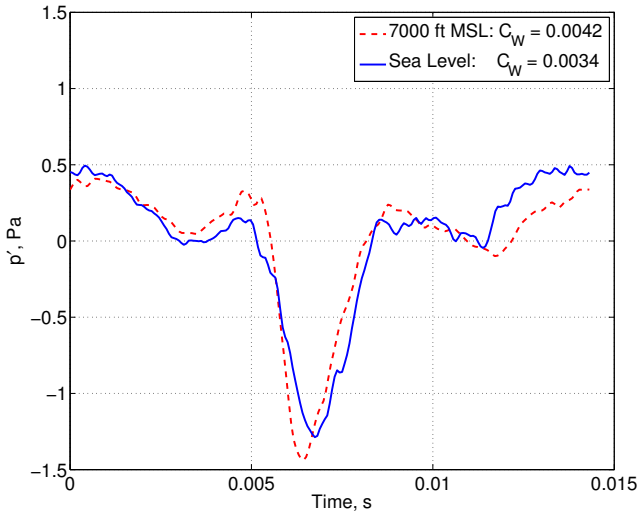

Fig. 11. Out-of-plane tail rotor averaged pressure time history.

At observer angles directly ahead of the helicopter and near the plane of the rotor, thickness noise amplitudes increase with decreasing ambient density for constant indicated airspeed flight. An increase of approximately 5 dB was observed over 7000 ft of altitude change. Thickness noise amplitudes were found to scale well with the effective hover tip Mach number, M_{H_e}, defined by Gopalan. In other radiation directions, both out of the plane of the rotor and in-plane to either side of the front of the vehicle, loading noise has a strong contribution to OASPL. Matching M_{H_e} alone is not sufficient to match low frequency noise levels in these directions; i.e., the amplitude and directivity of noise are shown to have a strong dependence on the weight coefficient, C_W, of the vehicle. Low frequency loading noise levels were observed to decrease by 6 dB in some directions as C_W increased by 24%, suggesting that these changes in loading noise are due to more complex changes in the operating condition of the rotor than a simple "scaling" of noise levels by the increase in thrust would indicate.

Blade-Vortex Interaction noise radiation was also shown to vary in magnitude and direction with changing ambient conditions. A 4 dB decrease in A-weighted noise levels was observed in the peak BVI radiation direction between the sea level and 7000 ft elevation test sites for flight conditions at the same indicated airspeed, gross weight, and similar flight path angles. Although flying such a dimensionally-defined flight condition results in a constant wake skew angle, χ, significant changes in the main rotor advance ratio, μ, can result from maintaining indicated airspeed as ambient air density changes. These changes in μ result in a change in the radiation direction and amplitude of BVI noise. BVI amplitudes may increase or decrease with changes in altitude, following Ref. 15.

During routine acoustic testing of helicopters, collecting data spanning a wide range of the nondimensional governing parameters of helicopter noise at a single test site is usually not possible. Using data collected at the sea level test site, a nondimensional FRAME model of the AS350 helicopter was constructed. This model was then applied to estimate the noise radiation characteristics of the helicopter under different ambient conditions than those at which the calibration data were obtained. The FRAME model was shown to accurately reflect the changes in noise levels and directivity caused by changes in the ambient conditions.

These findings have implications for the acoustic modeling of helicopters, especially the empirical source noise modeling commonly used in land-use and mission planning tools, such as RNM. Noise data collected under one set of ambient conditions cannot be directly applied to predict noise radiation flight conditions at the same airspeed and gross weight under other ambient conditions. Because the changes in directivity and amplitude of the different rotor harmonic noise sources vary in different, and often nonlinear, ways, no simple empirical model can be used to "correct" the data to other ambient conditions. However, by classifying the data in terms of the nondimensionally defined parameters that govern helicopter harmonic noise radiation, measured noise levels can be scaled to conditions with different atmospheric conditions and the same nondimensionally defined parameters. In most cases, it will not be practical to collect noise measurements at all nondimensionally defined operating conditions that may be flown under different ambient conditions. By using measured data to inform a physics-based model of the helicopter noise sources, accurate estimates of noise radiation at other nondimensional operating conditions, and hence ambient conditions, can be obtained. These results indicate that conventional empirical noise modeling methods should be used with caution, as they may produce erroneous results when predicting noise at ambient conditions significantly different than those where the original measurements were acquired.

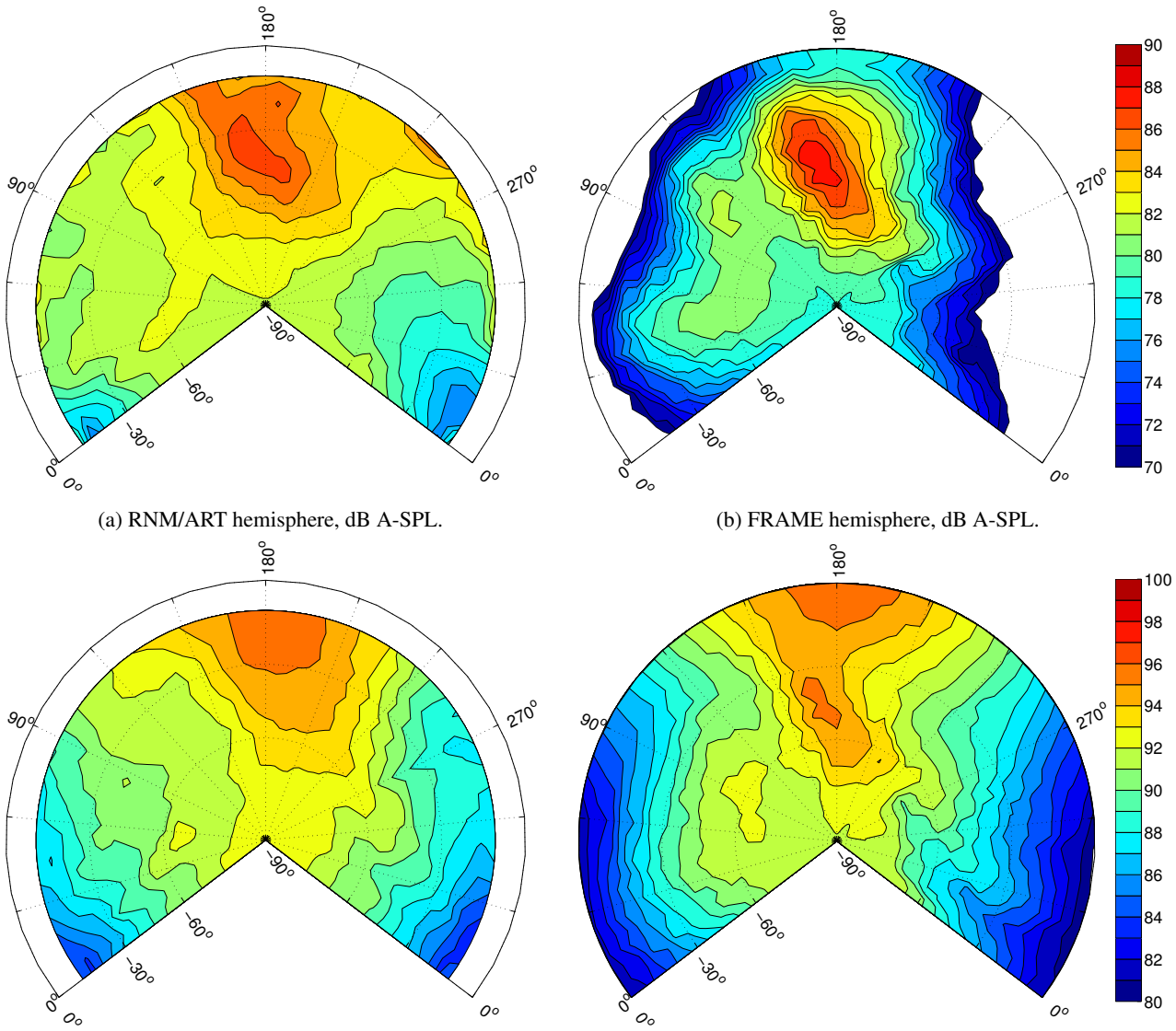

(a) RNM/ART hemisphere, dB A-SPL.

(b) FRAME hemisphere, dB A-SPL.

(c) RNM/ART hemisphere, dB OASPL.

(d) FRAME hemisphere, dB OASPL.

Fig. 12. Measured (RNM/ART) and predicted (FRAME) noise level contours for γ = -5.3°, 87.2 KIAS descending flight condition at sea level. W = 4113 lbf, C_W = 0.0035, M_{H_e} = 0.742.

ACKNOWLEDGMENTS

The authors would like to acknowledge Charles D. Smith, Analytical Mechanics Associates, for generating the RNM/ART hemispheres used in the paper, Michael E. Watts, NASA Langley Research Center, for preliminary analysis of the AS350 state data, and Gloria K. Yamauchi and Wayne Johnson, NASA Ames Research Center, for providing the original SA349/2 CAMRAD II model. Thanks are also extended to the other major contributors to the AS350 portion of the altitude variation flight test campaign: David A. Conner and James H. Stephenson, US Army, Nikolas S. Zawodny, NASA Langley Research Center, H. Keith Scudder and Andrew McCrea, Analytical Mechanics Associates, Gina G. Willink, and Benny K. Cheung, NASA Ames Research Center, and Samuel Nowden, Timothy West, Hector Ayala, and Scott Donley, Aris Helicopters.

APPENDIX: NONDIMENSIONAL TRIM MODEL

The nondimensional governing parameters for rotor harmonic noise are defined by the dimensional flight condition, ambient atmospheric conditions, and helicopter geometric characteristics. First, the advancing tip Mach number is defined by the rotor true airspeed, V, the hover tip speed, ΩR, and the ambient speed of sound, a_0:

$$M_{AT} = \frac{V + \Omega R}{a_0} \tag{8}$$

where ambient speed of sound in air can be expressed as a function of ambient temperature:

$$a_0 = \sqrt{\gamma_* R_* T_0} \tag{9}$$

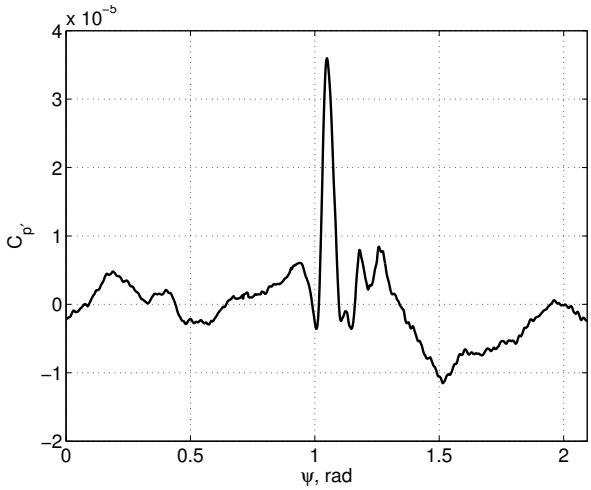

(a) Measured BVI pulse.

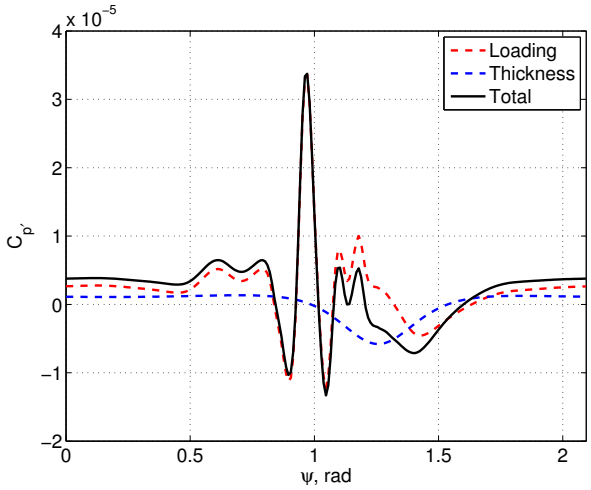

(b) FRAME calibrated BVI pulse.

Fig. 13. Comparison of the (a) measured and (b) calibrated BVI noise pulses radiated at 180° azimuth, -40° elevation. The predicted contributions of thickness and loading noise are also shown in (b).

The indicated airspeed is a function of freestream dynamic pressure, and is related to the true airspeed through air density using the following expression:

$$V_{IAS} = V\sqrt{\frac{\rho_0}{\rho_{SL}}} \tag{10}$$

Likewise, the rotor advance ratio is the ratio of the true airspeed to the hover tip speed.

$$\mu = \frac{V}{\Omega R} \tag{11}$$

The thrust coefficient is the nondimensionalization of rotor thrust with respect to a reference dynamic pressure, calculated from the rotor tip speed and ambient air density, and a reference area taken as the rotor disk area.

$$C_T = \frac{T}{\rho_0 A(\Omega R)^2} \tag{12}$$

For the helicopter main rotor in steady flight, thrust can be assumed equal to weight, defining an equivalent weight coefficient, C_W for the entire vehicle.

$$C_W = \frac{W}{\rho_0 A(\Omega R)^2} \approx C_T \tag{13}$$

Lastly, the rotor wake skew ratio, χ, is the ratio between the nondimensional inflow perpendicular to the rotor tip path plane, both freestream and induced, to the component of the advance ratio tangential to the rotor tip-path-plane, i.e.:

$$\chi = \frac{\lambda_i - \mu_z}{\mu_x} \approx \frac{\lambda}{\mu} \tag{14}$$

where the induced inflow ratio, λ_i, can be expressed from momentum theory as:

$$\lambda_i = \frac{C_T}{2\sqrt{(\mu_z + \lambda_i)^2 + \mu_x^2}} \tag{15}$$

and the x and y components of the advance ratio, μ, as:

$$\mu_x = \mu\cos\alpha \tag{16}$$

$$\mu_z = \mu\sin\alpha \tag{17}$$

In order to solve this expression, the rotor tip-path-plane angle of attack, α, must be estimated. Assuming the rotor thrust is normal to the tip-path-plane, and that the angle of attack is small, the following expression for α can be obtained through a longitudinal force balance of the helicopter along the wind axes:

$$\alpha = -\frac{D}{W} - \frac{H}{W} - \gamma \tag{18}$$

The drag-to-weight and H-force-to-weight ratios can be rewritten in terms of other nondimensional parameters as follows:

$$\frac{D}{W} \approx \frac{f}{A}\frac{\mu^2}{2C_W} \tag{19}$$

$$\frac{H}{W} \approx \frac{\sigma c_{d_0}}{8}\frac{1+4.6\mu^2}{\mu C_W} \tag{20}$$

Other aerodynamic drag forces, such as the drag of the horizontal and vertical stabilizers, may be treated separately from the effective flat plate drag of the fuselage, f/A, and those terms similarly nondimensionalized as a function of μ and C_W, as well as the aerodynamic angles of attack and sideslip. Likewise, the tail rotor H-force may be handled in a manner similar to that of the main rotor.

From these basic definitions of the nondimensional governing parameters, a fully nondimensional trim solution can be developed by balancing the six forces and moments of the helicopter in steady flight. First, the longitudinal, H, and lateral forces, Y, generated by the rotor can be put into a nondimensional form in the same way as the rotor thrust coefficient, C_T, was defined. Under the assumptions of uniform inflow and only including the first harmonic rigid blade flapping motions, the following expressions for these forces can be determined,

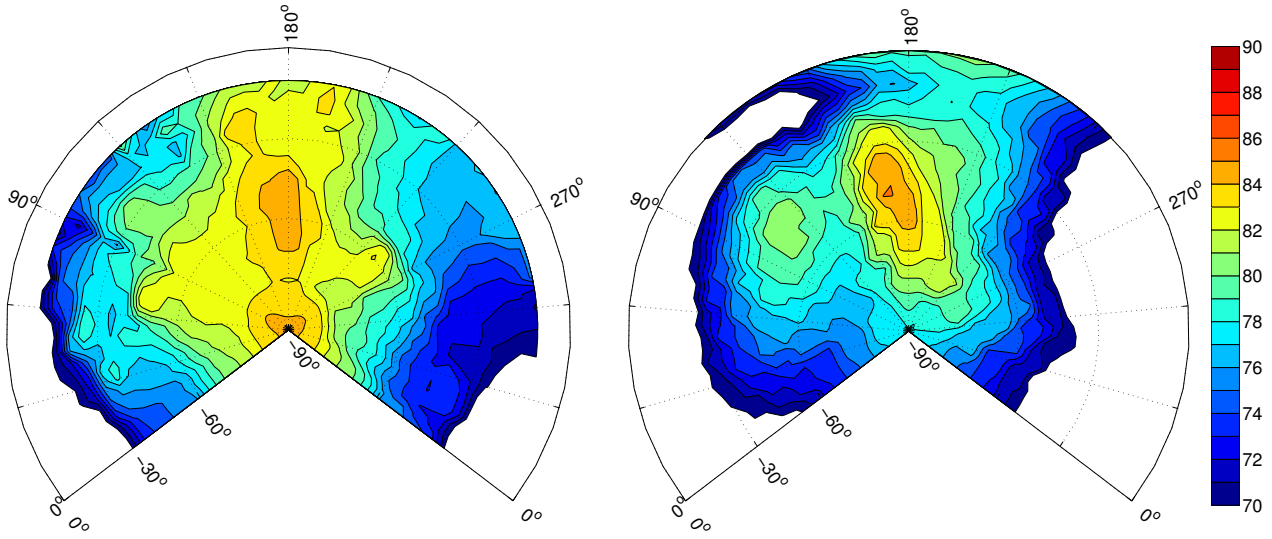

(a) RNM/ART hemisphere, dB A-SPL.

(b) FRAME hemisphere, dB A-SPL.

Fig. 14. Measured (RNM/ART) and predicted (FRAME) noise level contours for γ = -5.7°, 86.5 KIAS descending flight condition at 7000 ft MSL altitude. W = 4050 lbf, C_W = 0.0043, M_{H_e} = 0.765.

as a function of the governing parameters, nondimensional helicopter blade constants, the rotor controls, and the rotor flapping motion:

$$C_H = \frac{\sigma a}{2}\left[\frac{1}{2}\mu\lambda(\theta_0+\frac{1}{2}\theta_{tw})-\frac{1}{6}\beta_0\theta_{1c} +\frac{1}{4}\theta_{1s}\lambda+\frac{1}{4}\mu\beta_0^2\right]+\frac{\sigma c_{d_0}}{4}\mu \tag{21}$$

$$C_Y = -\frac{\sigma a}{2}\left[\frac{3}{4}\mu\beta_0(\theta_0+\frac{2}{3}\theta_{tw})+\frac{1}{4}\lambda\theta_{1c} +\frac{1}{6}\beta_0\theta_{1s}\left(1+3\mu^2\right)-\frac{3}{2}\mu\beta_0\lambda\right] \tag{22}$$

Next, the rotor blade flapping motion can be solved under the same set of assumptions, resulting in the following expressions for the rotor blade coning and first-harmonic flapping Fourier coefficients. The following expression determines the rotor blade coning:

$$\beta_0 = \frac{\gamma_b}{\nu_\beta^2}\left[\frac{\theta_0}{8}\left(1+\mu^2\right)+\frac{\theta_{tw}}{10}\left(1+\frac{5}{6}\mu^2\right) +\frac{\mu}{6}\left(\theta_{1s}+\beta_{1c}\right)-\frac{\lambda}{6}\right]+\frac{\omega_\beta^2}{\nu_\beta^2}\beta_p \tag{23}$$

Several new nondimensional parameters are introduced in this expression relating to the dynamics of the blades. ν_β is the rotating flapping frequency of the blades, relative to the rotor rotational speed, Ω, which is a function of the effective hinge offset of the rotor and the rotor blade mass properties and, therefore, remains constant regardless of ambient atmospheric conditions, at least for conventional rotors without pitch-flap coupling. Likewise, the non-rotating flapping frequency, ω_β, also remains constant. ω_β is zero for an articulated rotor and depends on the blade root stiffness and mass for a hingeless rotor with precone angle, β_p. γ_b is the Lock number, which represents the ratio between the rotor blade aerodynamic forces and the inertial forces. Because it is a function of aerodynamic forces, it will vary directly in proportion to changes in the ambient atmospheric density, ρ_0. However, for the range of air density experienced during typical helicopter operations, the effects of this parameter on the overall trim of the vehicle are expected to be small. (See Table 1 for CAMRAD II trim solutions under various ambient conditions.)

By balancing the longitudinal and lateral forces and moments, similar expressions for the longitudinal and lateral flapping coefficients can be obtained:

$$\beta_{1c} = \frac{-\frac{\bar{x}_c}{\bar{h}}+\frac{C_{M_y}}{\bar{h}C_W}+\frac{C_H}{C_W}}{1+\frac{\frac{\sigma a}{\gamma_b}\left(\nu_\beta^2-1\right)}{2\bar{h}C_W}} \tag{24}$$

$$\beta_{1s} = \frac{\frac{\bar{y}_c}{\bar{h}}-\frac{C_{M_x}}{\bar{h}C_W}+\frac{C_Y}{C_W}}{1+\frac{\frac{\sigma a}{\gamma_b}\left(\nu_\beta^2-1\right)}{2\bar{h}C_W}} \tag{25}$$

where C_{M_y} is the pitching moment coefficient of the fuselage, which is nondimensionalized by $\rho_0 A\left(\Omega R\right)^2 R$, similar to the force coefficients. C_{M_x} is likewise the rolling moment coefficient of the fuselage. These coefficients lump together the effects of all of the aerodynamic surfaces of the fuselage. Because they are defined with respect to a reference dynamic pressure, they remain constant with varying density provided all other parameters—such as advance ratio and angles of attack and sideslip—also remain constant. The nondimensional mast height, $\bar{h}$, and the longitudinal and lateral center-of-gravity

locations, $\bar{x}_c$ and $\bar{y}_c$, are geometric and remain constant with varying ambient conditions.

Next, the rotor torque coefficient, defined in a similar way to the fuselage moment coefficients, is calculated with the following expression:

$$C_Q = \frac{\sigma}{2}\left[\left(\frac{\theta_0}{3}+\frac{\theta_{tw}}{4}-\frac{\lambda}{2}\right)\lambda - \frac{\beta_{1c}^2+\beta_{1s}^2}{8} + \frac{c_{d_0}}{4a}\left(1+\mu^2\right)\right] \tag{26}$$

Finally, given the expressions accounting for all forces and moments, the trim controls can be determined. First, the main rotor torque is balanced by the tail rotor thrust, located $\bar{l}$ main rotor radii behind the main rotor hub, such that:

$$(C_T)_{TR} = \frac{C_Q}{\bar{l}} \tag{27}$$

where the tail rotor thrust required, $(C_T)_{TR}$, is nondimensionalized in this expression in terms of the main rotor parameters, $\rho_0 A\left(\Omega R\right)^2$.

Next, the main rotor controls are defined in terms of the nondimensional governing parameters, rotor geometry, mass, and aerodynamic constants, and the previously solved flapping coefficients.

$$\theta_0 = \frac{1}{1-\mu^2+\frac{9}{4}\mu^4}\left[\frac{6C_W}{\sigma a}\left(1+\frac{3}{2}\mu^2\right) - \frac{3}{4}\theta_{tw}\left(1-\frac{3}{2}\mu^2+\frac{3}{2}\mu^4\right)+\frac{3}{2}\lambda\left(1-\frac{\mu^2}{2}\right) + \frac{12}{\gamma_b}\mu\left(\nu_\beta^2-1\right)\beta_{1s}\right] \tag{28}$$

$$\theta_{1s} = -\beta_{1c} + \frac{1}{1+\frac{3}{2}\mu^2}\left[\frac{8}{\gamma_b}\left(\nu_\beta^2-1\right)\beta_{1c} - \frac{8}{3}\mu\left(\theta_0+\frac{3}{4}\theta_{tw}-\frac{3}{4}\lambda\right)\right] \tag{29}$$

$$\theta_{1c} = \beta_{1s} + \frac{1}{1+\frac{\mu^2}{2}}\left[\frac{8}{\gamma_b}\left(\nu_\beta^2-1\right)\beta_{1s}+\frac{4}{3}\mu\beta_0\right] \tag{30}$$

Lastly, the rotor fuselage pitch and roll attitude may be solved:

$$\theta = \theta_s + \frac{\frac{\bar{x}_c}{h} - \frac{C_{M_y}}{\bar{h}C_W} - K\frac{C_H}{C_W}}{1+K} - \frac{1}{2}\frac{f}{A}\frac{\mu^2}{C_W} \tag{31}$$

$$\phi = \phi_s + \frac{\frac{\bar{y}_c}{h} - \frac{C_{M_x}}{\bar{h}C_W} - K\frac{C_Y}{C_W}}{1+K} + \frac{C_Q}{\bar{l}C_W} \tag{32}$$

where

$$K = \frac{\left(\nu_\beta^2-1\right)/\gamma_b}{2h\frac{\bar{C}_W}{\sigma a}} \tag{33}$$

In practice, these equations are not solved analytically and trim solutions are achieved through numerical iteration until the trim controls converge. When these equations are put into a nondimensional form, and the flight condition defined in terms of the nondimensional governing parameters defined by Eqs. 8, 11, 13, and 14, only the Lock number, γ_b, varies with varying ambient temperature or density. Across the range of γ_b experienced at all practical density-altitudes, the effect of Lock number on trim, and the resulting acoustic state of the rotor, is expected to be small. The equations developed in this Appendix for blade flapping motion and trim controls are used directly in the trim solutions procedure used by the nondimensional FRAME model; however, the aerodynamic forces generated by the rotor are calculated directly through integration of the FRAME airloads model instead of the analytical expressions shown in Eqs. 21, 22, and 26.

One key parameter necessary to accurately estimate values of the wake skew angle, χ, using Eq. 19, is the effective flat plate drag area of the fuselage, f. Working under the assumption that rotor "H-force" and fuselage moment are relatively small, Eq. 31 can be simplified to:

$$\theta = -\frac{f}{2C_W A}\mu^2 + \theta_s \tag{34}$$

This simple expression can then be fit to measurements of the pitch attitude of the helicopter's fuselage across a range of advance ratios, μ, in order to solve for the unknown effective flat plate drag area and shaft tilt angle. This process was conducted for the AS350 SD1 helicopter using measured data for a level flight speed sweep conducted at the 4000 ft elevation test site. The fitted model, and resulting flat plate drag area estimate is plotted in Fig. 15. The nondimensional drag value of $f/A = 0.0071$ corresponds to a dimensional value, f, of 7.26 ft^2, which is typical for an aerodynamically clean helicopter of this size. This value was used to model the parasite drag of the AS350 airframe in both the FRAME and CAMRAD II models of the helicopter.

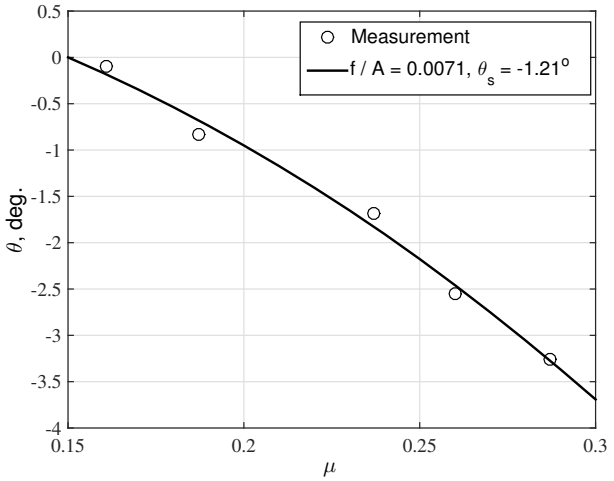

Fig. 15. Effective flat plate drag area estimate from measured vehicle pitch data.

REFERENCES

[1]Connor, T. L., "Integrated Noise Model-The Federal Aviation Administration's computer program for predicting noise exposure around an airport," Inter-noise 80: Noise control for the 80's, Miami, FL, Jan 1980.

[2]Lucas, M. J. and Marcolini, M. A., "Rotorcraft Noise Model," AHS Technical Specialists' Meeting for Rotorcraft Acoustics and Aerodynamics, Williamsburg, VA, October 1997.

[3]Conner, D. A. and Page, J. A., "A Tool for Low Noise Procedures Design and Community Noise Impact Assessment: The Rotorcraft Noise Model (RNM)," Heli Japan, Tochigi, Japan, 2002.

[4]Browne, R. W., Munt, R. M., Simpson, C. R., and Williams, T., "Prediction of Helicopter Noise Contours for Land Use Planning," 10th AIAA/CEAS Aeroacoustics Conference, Manchester, Great Britain, 2004.

[5]Gervais, M., Gareton, V., Dummel, A., and Heger, R., "Validation of EC130 and EC135 Environmental Impact Assessment using HELENA," American Helicopter Society 66th Annual Forum, Phoenix, AZ, May 2010.

[6]Guntzer, F., Spiegel, P., and Lummer, M., "Genetic Optimizations of EC-135 Noise Abatement Flight Procedures using an Aeroacoustic Database," 35th European Rotorcraft Forum, Hamburg, Germany, September 2009.

[7]Fleming, G. G. and Rickley, E. J., "Heliport Noise Model, HNM. Version 2.2 (User's Guide)," DOT-VNTSC-FAA-94-3, Federal Aviation Administration, February 1994.

[8]Fleming, G. G., Plotkin, K. J., Roof, C. J., Ikelheimer, B. J., and Senzig, D. A., "Assessment of Tools for Modeling Aircraft Noise in the National Parks," Technical Report, FICAN, March 2005.

[9]Schmitz, F. H., Boxwell, D. A., Léwy, S., and Dahan, C., "Model- to Full-Scale Comparisons of Helicopter Blade-Vortex Interaction Noise," *Journal of the American Helicopter Society*, Vol. 29, (2), 1984, pp. 16–25.
doi: 10.4050/JAHS.29.16

[10]Boxwell, D. A., Schmitz, F. H., Splettstoesser, W. R., and Schultz, K. J., "Model Helicopter Rotor High-Speed Impulsive Noise: Measured Acoustics and Blade Pressures," TM 85850, National Aeronatics and Space Administration, September 1983.

[11]Boxwell, D. A., Schmitz, F. H., Splettstoesser, W. R., and Schultz, K. J., "Helicopter Model Rotor-Blade Vortex Interaction Impulsive Noise: Scalability and Parametric Variations," *Journal of the American Helicopter Society*, Vol. 32, (1), 1987, pp. 3–12.
doi: 10.4050/JAHS.32.3

[12]Ffowcs Williams, J. E. and Hawkings, D. L., "Sound generation by turbulence and surfaces in arbitrary motion," *Philosophical Transactions of the Royal Society of London*, Vol. 264, May 1969, pp. 321–342.

[13]Yamauchi, G. K., Signor, D. B., Watts, M. E., Hernandez, F. J., and LeMasurier, P., "Flight Measurements of Blade-Vortex Interaction Noise Including Comparisons With Full-Scale Wind Tunnel Data," *Journal of the American Helicopter Society*, Vol. 41, (4), 1996, pp. 291–301.
doi: 10.4050/JAHS.41.291

[14]International Organization for Standardization, "Standard Atmosphere," 2533:1975, ISO, 1975.

[15]Greenwood, E. and Schmitz, F. H., "Effects of Ambient Conditions on Helicopter Rotor Source Noise Modeling," *Journal of Aircraft*, Vol. 51, (1), January 2014, pp. 90–103.
doi: 10.2514/1.C032045

[16]Watts, M., Greenwood, E., and Stephenson, J., "Measurement and Characterization of Helicopter Noise at Different Altitudes," American Helicopter Society 72nd Annual Forum, West Palm Beach, FL, May 2016.

[17]Gopalan, G. and Schmitz, F. H., "Far-Field Near-In-Plane Harmonic Main Rotor Helicopter Impulsive Noise Reduction Possibilities," American Helicopter Society 64th Annual Forum, Montreal, Quebec, Canada, May 2008.

[18]Heffernan, R. and Gaubert, M., "Structural and Aerodynamics Loads and Performance Measurements of an SA349/2 Helicopter with an Advanced Geometry Rotor," TM 88370, NASA, November 1986.

[19]Heffernan, R., Precetti, D., and Johnson, W., "Vibration Analysis of the SA349/2 Helicopter," TM 102794, NASA, January 1991.

[20]Greenwood, E., *Fundamental Rotorcraft Acoustic Modeling from Experiments (FRAME)*, Ph.D. thesis, University of Maryland, January 2011.

[21]Greenwood, E. and Schmitz, F. H., "A Parameter Identification Method for Helicopter Noise Source Identification and Physics-Based Semi-Empirical Modeling," American Helicopter Society 66th Annual Forum, Phoenix, AZ, May 2010.

[22]Greenwood, E. and Schmitz, F. H., "Separation of Main and Tail Rotor Noise from Ground-Based Acoustic Measurements," *Journal of Aircraft*, Vol. 51, (2), February 2014, pp. 464–472.
doi: 10.2514/1.C032046

[23]Farassat, F., "Derivation of Formulations 1 and 1A of Farassat," TM-2007-214853, NASA, 2007.

[24]Lopes, L., "Compact Assumption Applied to the Monopole Term of Farassat's Formulations," 21st AIAA/CEAS Aeroacoustics Conference, Dallas, TX, June 2015.

[25]Beddoes, T. S., "A Wake Model for High Resolution Airloads," International Conference on Rotorcraft Basic Research, Research Triangle Park, NC, February 1985.

[26]van der Wall, B. G., "The Effect of HHC on the Vortex Convection in the Wake of a Helicopter Rotor," *Aerospace Science and Technology*, Vol. 4, (5), 2000, pp. 321–336.

[27]Bhagwat, M. J. and Leishman, J. G., "Generalized Viscous Vortex Core Models for Application to Free-Vortex Wake and Aeroacoustic Calculations," 58th Annual Forum of the American Helicopter Society, Montreal, Canada, June 2002.

[28]Landgrebe, A. J., "The Wake Geometry of a Hovering Helicopter Rotor and its Influence on Rotor Performance," *Journal of the American Helicopter Society*, Vol. 17, (4), 1972.

[29]Beddoes, T. S., "Practical Computation of Unsteady Lift," *Vertica*, Vol. 8, (1), 1984.

[30]Leishman, J. G., *Principles of Helicopter Aerodynamics*, Cambridge University Press, New York, second edition, 2006.